THE INFLUENCE OF NEW SEVERE PLASTIC DEFORMATION ON MICROSTRUCTURE, MECHANICAL, AND CORROSION PROPERTIES OF Mg-0.8Mn-0.5Ca ALLOY

M. Khani [a], G.R. Ebrahimi [b, *], H.R. Ezatpour [c], A. Momeni [d]

[a] Department of Materials and Polymer Engineering, Hakim Sabzevari University, Sabzevar, Iran
[b] Department of Materials and Metallurgical Engineering, Faculty of Engineering, Ferdowsi University of Mashhad, Mashhad, Iran
[c] Department of Engineering Sciences, Campus of New Technologies, Hakim Sabzevari University, Sabzevar, Iran
[d] Department of Materials Science and Engineering, Hamedan University of Technology, Hamedan, Iran

Abstract

In this research, the effect of accumulative extrusion bonding (AEB) on the microstructure and mechanical properties of Mg-0.8Mn-0.5Ca biocompatible alloy was investigated. The goal of this research was to develop the mechanical and corrosion properties of Mg-0.8Mn-0.5Ca alloy after ABE process as a novel severe plastic deformation process. The simulation of AEB process showed that the average effective strain per pass for channels with the internal angle of 120° was about 1.93. The average grain size was dramatically decreased from about 448.3 μm for the homogenized alloy to 1.55 μm for the 3-pass processed sample. Microstructural observations suggested a combination of continuous, discontinuous, and twinning-induced dynamic recrystallization as the major mechanisms of grain refinement. Tensile and compressive strengths were improved from 150 and 205 MPa to 330 and 301 MPa after three passes of AEB, indicating 2 and 1.5 times improvements, respectively. Tensile elongation decreased from 26% for the homogenized sample to 7.5% for the 3-pass processed sample due to the severe work-hardening, non-uniform strains, and inhomogeneous microstructure produced by the ABE process. Corrosion resistance in SBF solution was improved from 1.1 to 14.159 after three passes of ABE due to the presence of hydroxyapatite formed on the surface of the AEBed samples.

Keywords: Mg-0.8Mn-0.5Ca alloy; Accumulative extrusion bonding; Microstructure; Mechanical properties; Corrosion

1. Introduction

Recently, magnesium alloys have received much attention due to their high strength to weight ratio, desirable mechanical properties such as low young modulus (44 GPa) comparable to human bone marrow (17 GPa), high biocompatibility and great biodegradability [1]. These properties suggest the possibility of gradual absorption of the implant within the human body, which eliminates the costs of secondary surgery for removal of metallic implants [2]. However, the degradation rate of Mg alloys in physiological environments can be short which decreases mechanical properties in implants before restoration of the human tissue [3, 4]. Eqs. (1) and (2) illustrate the anodic and cathodic reactions during the degradation of Mg alloys, respectively:

$$Mg \rightarrow Mg^{2+} + 2e^- \tag{1}$$

$$2H_2O + 2e^- \rightarrow H_2 + 2OH^- \tag{2}$$

According to the reactions, OH^- ions from the cathodic reaction increase the pH of the solution which stabilizes the $Mg(OH)_2$. Based on the Eq. (3), the degradation rate of Mg alloys (P_i) is obtained having the corrosion current density (i_{Corr}) [5, 6, 7].

$$P_i = 22.85 \, i_{Corr} \tag{3}$$

The corrosion resistance (R_p) of the specimens can be calculated using the electrochemical parameters, i.e. β_a, β_c, and i_{Corr}, given by [5, 7]:

*Corresponding author: r.ebrahimi@um.ac.ir

$$R_p = \frac{\beta_a \beta_c}{2.3(\beta_a + \beta_c)i_{corr}} \qquad (4)$$

where the corrosion current density (i_{Corr}), corrosion potential (E_{Corr} V_{SCE}), Tafel cathodic slope (β_c), Tafel anodic slope (β_a), and corrosion rate (P_i) of each sample are extracted from the potentiodynamic polarization (PDP) tests.

These issues, such as high degradation rate and low strength, limit the comprehensive applications of magnesium implants [8]. Various techniques such as alloying [9-12], composite preparation [13-14], surface treatment [15], and use of severe plastic deformation (SPD) processes [16] have been utilized so far to overcome the drawbacks. Alloying elements must be carefully selected in the production of Mg alloys in order to avoid the release of toxic compounds in the body. Elements such as calcium (Ca), manganese (Mn), zinc (Zn), tin (Sn), and strontium (Sr) have been prioritized since they are considered as the nutrition elements [17-18]. If the Ca and Mn contents are selected correctly, it can help improve the mechanical and corrosion properties of Mg alloys along with benefiting the human body [19-22]. Ca has been shown to be effective in grain refining of the alloy which can improve the corrosion resistance. Presence of Ca up to 0.5 wt. % has a favorable effect on grain refinement, strength increase, and elongation improvement. The higher percentages result in the formation of undesirable Mg_2Ca phase, which acts as a crack source and declines the mechanical properties [23]. Mn can improve the corrosion resistance of Mg alloys by forming a passive layer on the surface. This layer prevents chloride ion diffusion into the Mg matrix. The amount of Mn for achieving the optimum of mechanical and corrosion properties in Mg alloys has been reported as 0.8 wt. % [24].

To prepare Mg-matrix composites, ceramic bioactive particles are commonly used [25-27]. Additionally, the formation of bioactive surface coatings including Ca-P [28], Si [29], and hydroxyapatite (HA) compounds [30] are proposed. As HA layer often forms on the surface grain boundaries, in fine grained alloys HA layer shows a more uniform distribution. Here, the SPD processes will be effective even on the performance of protective layers, like HA.

The SPD processes increase the grain boundary density by grain refinement, thereby improving strength and ductility. Various SPD processes have been proposed such as equal-channel angular pressing (ECAP) [31-32], multidirectional forging (MDF) [33], Dual Rolls Equal Channel Extrusion (DRECE) [34], and so on. Among these, ECAP is considered as the most effective SPD technique to produce porosity-free bulk ultrafine-grained materials. However, some studies have reported the reduction of strength after ECAP. It has been ascribed to the formation of a soft deformation texture during the process [35-37]. The combination of ECAP and extrusion simultaneously improves the strength by grain refinement [16]. Nevertheless, the inability to perform multiple passes to achieve finer structures is one of the limitations of this method. Four mechanisms have been related to the development of ultrafine microstructure during SPD processes of Mg alloys at high temperature:

(1) Discontinuous dynamic recrystallization (DDRX): DDRX has been suggested as the main mechanism for the formation of ultra-fine grains along the primary boundaries in Mg alloys. The DDRX is commonly seen in metals with low to medium stacking fault energy (SFE) such as Mg alloys. The extensive work hardening and abundant internal energy due to the aggregation of dislocations make the material prone to DDRX when strain reaches a critical value [38, 39]. The elongated grain boundaries can contribute to the nucleation of new DDRX grains by the mechanism that is called "strain-induced local grain boundary migration" (SIBM) [38-41]. In this mechanism, grain boundary locally bulges into the grain with larger stored energy and removes all dislocations in the swept volume. In the next step the dislocation-free volume is introduced as the DDRX nucleus and start to grow inside the deformed matrix. This process has been also proposed as the dominant mechanism during the hot deformation of Mg alloys. In most cases, SIBM gives rise to extensive grain boundary nucleation, which forms a necklace-like structure.

(2) Shear bands: generally, in all SPD processes, localized deformation is seen as the formation of shear bands. The flow localization in shear bands often degrades workability and may lead to premature fracture [41]. However, the strain path in SPD often alleviates the harmful effect of shear bands and therefore materials exhibit better resistance to fracture.

(3) Twinning: twin boundaries play a significant role in grain refinement of Mg alloys during SPD process. Twinning formation is controlled by temperature, alloying elements, strain rate, and the primary texture in Mg alloys. It has been understood that the formation of twins is the dominant mechanism of deformation in the early stages of SPD process in Mg alloys [43]. Twin boundaries significantly contribute to grain refinement during the first and second passes of the ECAP process [5]. One idea has been the twinning dynamic recrystallization (TDRX) [44]. In this mechanism, which is only seen in Mg alloys, the mutual intersection of primary twins leads to the formation of DRX nuclei. In the next step, the boundaries surrounding the nuclei turn into random high angle grain boundaries (HAGBs) with

increase in the applied strain. In fact, the nucleation phenomenon occurs by the TDRX mechanism, while the growth proceeds by the continuous dynamic recrystallization.

(4) Continuous dynamic recrystallization (CDRX): observing a duplex distribution of grain size in Mg alloy. In this mechanism, the dislocation forests formed during SPD process are recovered by nucleation of new grains to decrease internal energy [45].

According to the Hall-Petch equation (5), superior strengths can be achieved by grain refinement after the SPD processes. The large strains in the SPD processes refine subgrains and rotate them gradually into HAGBs. The new HAGBs act as strong obstacles against moving dislocations, leading to more work hardening and higher strengths [45]:

$$\sigma_y = k_y d^{-0.5} \quad (\sigma = \text{strength}, \ d = \text{grain size}) \tag{5}$$

In Mg alloys, SPD is necessary; because the conventional deformation processes cannot refine the microstructure as needed. Hence, the present study presents an introduction of a new accumulative extrusion bonding (AEB) process with 120°-angle channels, for the first time in the literature. It should be mentioned that various accumulative severe plastic deformations, such as accumulative rolling [47, 48] and accumulative pressing [49], have been introduced before and used for sheets. Hence, in this research, the biomedical grade Mg-0.8Mn-0.5Ca was prepared by the mechanical stir casting technique and further processed by AEB. Then the mechanical and corrosion properties of AEBed Mg-0.8Mn-0.5Ca alloy were evaluated by the standard tensile, potentio-dynamic polarization (PDP), and the hydrogen evolution immersion (HEI) tests.

2. Materials and methods

Mg ingots with 99.9 % purity, Mn flakes with 99.9 % purity, and Ca with 99 % purity were used for the alloy preparation in this research. In order to produce Mg-0.8Mn-0.5Ca alloy, a total amount of 350 g Mg, 2.9 g Mn, and 1.8 g Ca were inserted into an electrical furnace equipped with mechanical stirrer, heated to 750 °C and held for 15 min to melt the materials under Ar atmosphere. The casting temperature was 750 °C. Then, the molten alloy was mixed by a mechanical stirrer at 350 rpm for 10 min under argon to produce the alloy. Finally, the melt was poured into a steel mold preheated at 400 °C. Final chemical composition was determined by inductively coupled-plasma atomic emission spectrometry (ICP-AES).

The as-cast samples were homogenized under Ar atmosphere at 450 °C for 24 h. Afterwards, specimens with $80 \times 30 \times 15 \ mm^3$ dimensions were prepared by

CNC wire-cut machine from the homogenized ingot. The prepared specimens were preheated at 400 °C for 10 min and then inserted into the AEB die (Fig. 1) and pressed at strain rate of 1 mm/s.

The die cross section was reduced from 30×15 mm^2 in the entry of channel to $15 \times 15 \ mm^2$ at exit and the channel angle was 45° (Fig. 2(a)). The inside and outside angles of intersection between the entry and exit channels were $\Phi = 120°$ and $\Psi = 10°$, respectively (Fig. 2(b)). The die was heated up to 400 °C and the mixture of graphite and refractory grease was employed as lubricant. The die was mounted on a shoe and the ram was pressed by 25-ton Zwick/Roell universal tensile/compression machine (model Z250, Sweden). After this, the processed samples were cooled in air. For the next pass, the processed billets were cleaned by immersion in acetone for 10 min to remove remaining lubricant and dust. To improve the bonding between billets, they were brushed by a wire brush to remove the oxide films and roughen the surface (Fig. 2(c)). At this stage, the surface roughness reached Ra ≈ 6.1 μm (Ra was measured by a surface profilometer). For the next pass, the specimens were rotated 90 degrees along the horizontal axis. Both ends of samples were restrained by an instant adhesive and then inserted into the die (Fig. 2(d)).

Finite element analysis (FEA) of the introduced deformation process was studied using the Deform-3D V.5 software in order to calculate the effective strain in one pass of ECAP (ε_{ECAP}) and extrusion process ($\varepsilon_{extrusion}$) based on Eqs. (6) and (7). The average effective strain (ε_{ave}) was obtained by Eq. (8). The friction coefficient at the interface between the billet and the die was assumed to be 0.1. In addition, the magnitude of ram speed was set as 1 mm/s. The 4-
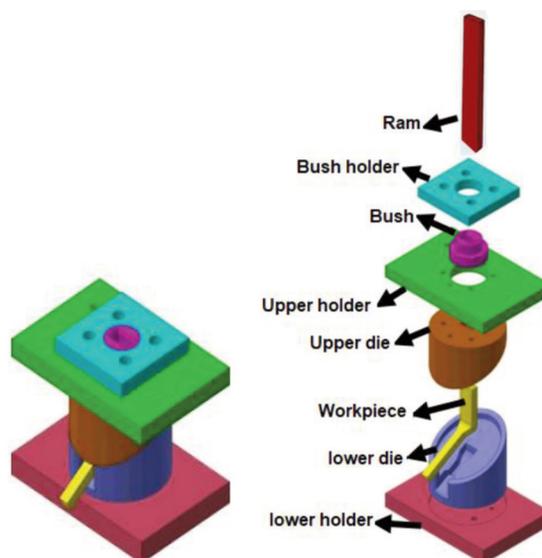
Figure 1. Schematic illustration of ABE set up
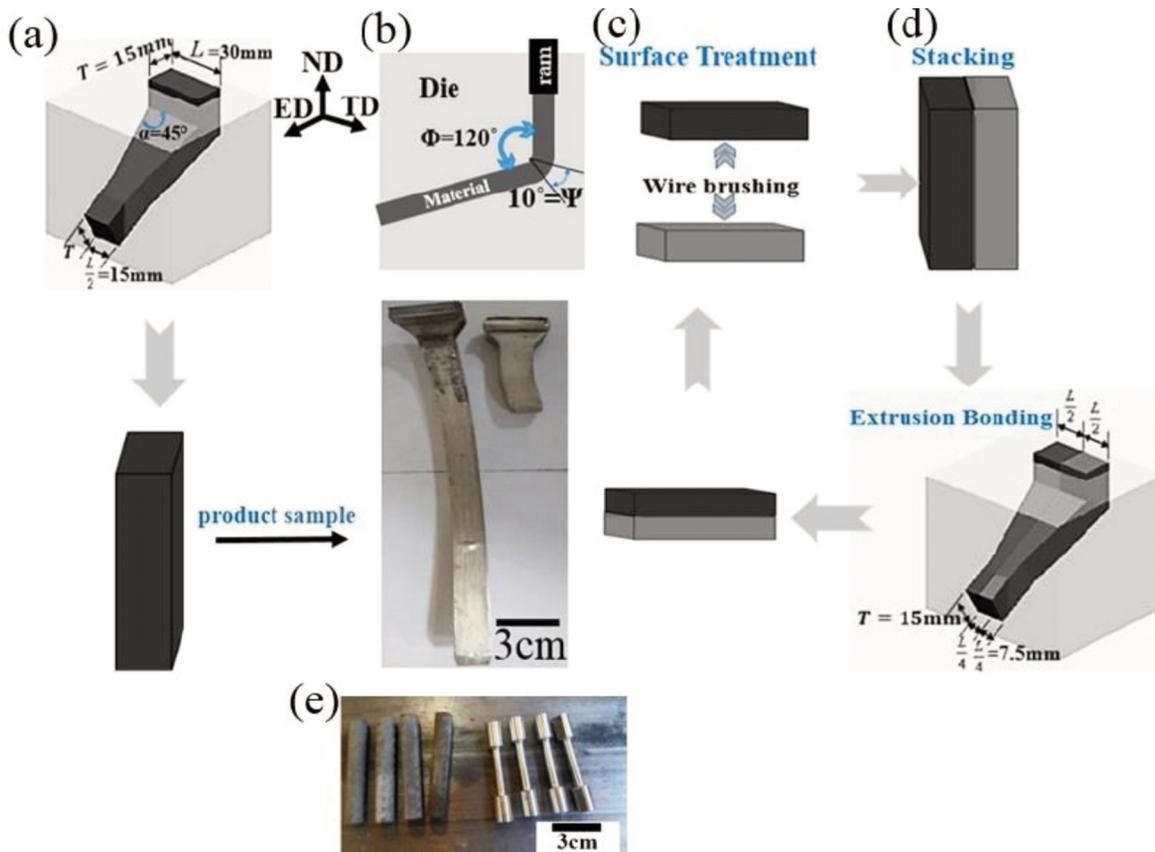
Figure 2. *Schematics of the die dimensions and sample feeding in the accumulative extrusion bonding (AEB) using 120°-angle channels process at first pass, (a) the die cross section, (b) the inside and outside angles of intersection between the entry and exit channels, (c) wire brushing and (d) second and third passes*

node linear tetrahedral elements were used to mesh the billet.

$$\varepsilon_{ECAP} = \frac{1}{\sqrt{3}}\left(2Cot\left(\frac{\Phi}{2}+\frac{\psi}{2}\right)+\psi\left(Cosec\left(\frac{\Phi}{2}+\frac{\psi}{2}\right)\right)\right) \quad (6)$$

$$\varepsilon_{extrusion} = Ln\frac{A_0}{A_f} \quad (7)$$

$$\varepsilon_{ave} = \frac{\sum_{i=1}^{n}\varepsilon i}{n} \quad (8)$$

To study the mechanical properties of the AEBed samples, tensile and compression tests were carried out according to ASTM-E8 (Gauge length: 45 mm, Diameter: 9 mm as shown in Fig. 2(e)) and ASTM-E9 standards (height/diameter: 1.5), respectively. The tests were implemented using universal tensile/compression machine (model Z250, Sweden) with strain rate of 0.01 s^{-1}. Three specimens were used for each condition.

The microstructures of homogenized (before AEB) and processed (after AEB) samples were revealed after standard metallographic preparation method. Firstly, the specimens were cut along the

extrusion transverse direction (ED-TD) and ground with 320–4000 silicon carbide (SiC) grit papers and mirror polished on the cloth using diamond compound. Then, the ground specimens were etched using a solution of 1.5 g picric acid, 25 ml ethanol, 5 ml acetic acid, and 10 ml distilled water for 5-10 s. The microstructures (from center of specimens) and fracture surfaces of the samples were examined using Olympus optical microscope (model GX51, Japan) and field emission scanning electron microscope (FESEM) TESCAN (model MIRA3, Czech Republic) equipped with energy dispersive X-ray spectroscopy (EDS). The average grain size of the samples was measured according to ASTM E112-96 standard by linear intercept method. In this standard, we counted the number of grains intercepted by test lines on a microstructure image of the specimen. The number of grain boundary intersections per unit length determined the grain size. Three specimens were used for each condition.

The biocorrosion behavior of the samples was investigated by the HEI and electrochemical tests. For hydrogen evolution test the samples with 10×10×4 mm^3 dimensions were ground by 5000 grit sand paper

and placed in SBF solution for 168 h at 37±1 °C (Table 1). The volume of generated hydrogen from the specimens was measured by the burette connected to a funnel on the top of the sample and recorded with time. The PDP tests were done by immersing the mounted samples (10×10 mm²) in the SBF solution. The contact surface of samples was connected by a copper wire to Ivium-n-stat potentiostat device (model CompactStat, Netherlands) with three-electrode system. In this system the reference electrode was Ag/AgCl and platinum was the counter electrode. Primarily, the samples were exposed to open circuit potential (OCP) for 1800 s before the PDP test to achieve relative stability. The potential of working electrode was measured with respect to the reference electrode from -250 to +250 mV at scan rate of 1 mV/s. The corrosion mechanism was studied via plotting the PDP graphs and the corrosion products and corroded surface were characterized by FESEM.

3. Results and discussions
3.1. Accumulative extrusion bonding

Fig. 3(a) shows the force-displacement curves of ABEed samples at different passes. As is seen, the force increased with increment of the passes number due to the strength increase. Also, the curves presented two distinct peaks during process while the first peak was related to ECAP process and the second peak indicated the start of extrusion process.

The effectiveness of grain refinement in SPD processes crucially depended on the amount of strain applied to the test specimens. Fig. 3(b) exhibits the finite element results showing the distribution and amount of average effective plastic strain in channels with 120 angle (φ) based on the Eq. (8). As the strain contour showed, there was a strain gradient in the cross-section of samples. The effective plastic strain was maximized at the outer section, where the material bore severe shear against the die surface. At the inner part, however, less friction decreased the strain by 1/3 of its value at the surface. Hence,

Table 1. Chemical composition of SBF solution

Reagent	Amount
NaCl	7.996 g
NaHCO$_3$	0.350 g
KCl	0.224 g
K$_2$HPO$_4$.3H$_2$O	0.228 g
MgCl$_2$.6H$_2$O	0.30 g
HCl(1.0M)	40 ml
CaCl$_2$	0.278 g
Na$_2$SO$_4$	0.071 g
Tris buffer ((CH$_2$OH)$_3$CNH$_2$)	6.057 g

according to the simulation results, the average effective plastic strain during one pass of AEB process was approximately about 1.93. This value was nearly two times of the average effective plastic strain reported for one pass of conventional ECAP (about 1.1) [50, 51]. Using Eq. (6), proposed for ECAP, at Φ =120° and Ψ =10°, the strain of 1 was obtained during each pass and according to Eq. (7) the lowest strain for per pass happened during simple extrusion with 2:1 ratio, i.e. about 0.7. This comparison implied that AEB with the highest strain in per pass was more capable compared to simple extrusion and conventional ECAP to refine the microstructure of metallic materials.

Fig. 3(c) shows the layers stacked after 3-pass of AEB and the morphology of their interface has been outlined in Fig. 3(d, e). As observed in Fig. 3(c), the thickness of interface between layers was about 10 mm. In most parts of the interface appropriate bonding between the layers was obtained. The bonding of consecutive layers by AEB occurred in three stages [52]: (a) fracture of the interface layers by the severe deformation and their elongation alongside the extrusion direction, (b) extrusion of the underlying materials through widening cracks in the surface layers from both sides of the interface, and (c) formation of atom-to-atom bonds between the layers.

In the entry channel, the bonding between the surfaces occurred to some extent due to the pressure of die walls. Then, the bonding was strengthened during passing through the exit channel. The number of layers in AEB process (L) was obtained by:

$$L = 2^{n-1} \qquad (9)$$

where, n is the pass number. In parallel with the increase in the number of layers (L), the thickness of layers (T) reduced as follows:

$$T = \frac{T_0}{2^{n-1}} \qquad (10)$$

where, T_0 is the thickness of initial sample. Taking n= 3 (number of passes in this research) and T_0= 15 mm (the initial thickness), L and T were calculated as 4 and 3.75 mm, respectively which was in agreement with Fig. 3(c).

3.2. Microstructure characterizations

Fig. 4 displays the microstructure and grain size of different sections of the AEBed samples. The micrographs clearly show the development of microstructure in different stages of the process including initial microstructure (Fig. 4(a)), before ECAP (Fig. 4(b)), after ECAP (Fig. 4(c)), and after extrusion (Fig. 4(d)). A comparison between Figs. 4(c) and 4(d) revealed that the grains were subjected
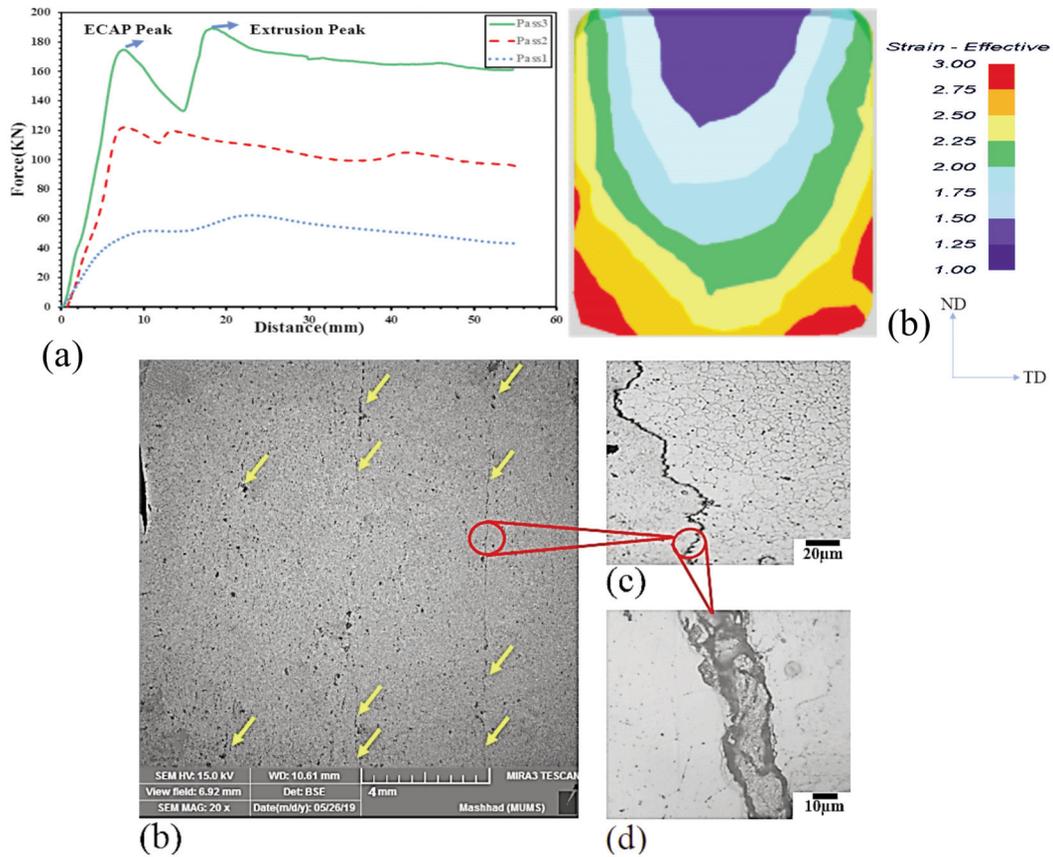
Figure 3. (a) The force-displacement plots of ABEed samples at different passes, (b) the distribution and amount of average effective plastic strain in channels with 120 angle (φ), SEM micrograph showing the layers joint by AEB and (c, d) morphology of layers interface in two magnifications
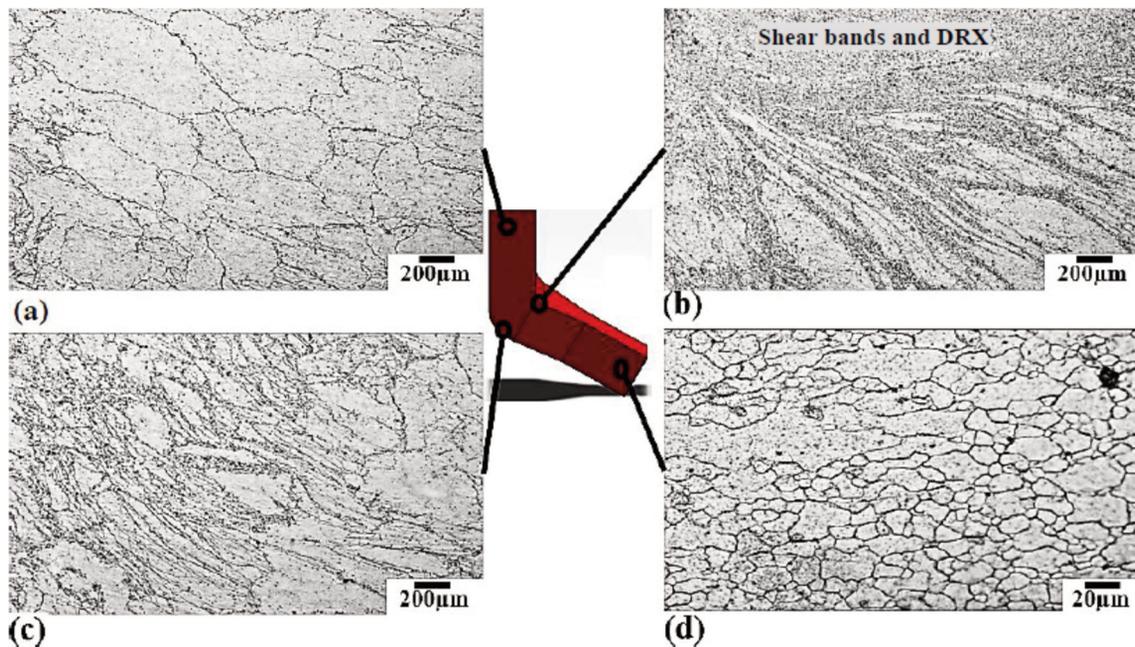
Figure 4. Optical micrographs displaying the microstructures of Mg-0.8Mn-0.5Ca alloy after one-pass of AEB: (a) at the starting point (homogenized alloy), (b, c) the top and bottom of ECAP region, and (d) after ECAP and extrusion

to larger strain and were evidently more elongated near the internal angle of channels. This indicated that there was a gradient of strain in the ECAP stage, so that the strain rose from the bottom to the top of channel. Based on the observations in Fig. 4, the first pass of AEB refined the average grain size of Mg-0.8Mn-0.5Ca alloy from 448 mm at the start of process to 24.26 μm at the end; this was about 95 % reduction in grain size. Fig. 4(b, c) shows that very fine new grains were nucleated on the prior grain boundaries at severe deformed zones while the nucleation of new grains did not begin outside the zones. It appears that dynamic recrystallization was the main mechanism for the formation of fine grains in the ECAP region. In agreement with the observations in Fig. 4(b, c) in ABEed Mg alloy, other microstructural studies on Mg alloys under SPD indicated that larger strains localized in the shear bands boosted the kinetics of DRX [53-55]. The pioneering recovery and recrystallization in shear bands played essential roles in grain refinement during ECAP [56].

Fig. 5(a) shows the bulged grain boundaries through SIBM in the lower part of ECAP region. Fig. 5(b) supports the idea of SIBM, showing the necklace

structure of DDRXed grains alongside the primary grain boundaries in the ECAP region. Fig. 5(c and d) illustrate the formation of some twin boundaries in the ECAP region in the studied material. As arrows pointed to the appearance of twins inside the old deformed grains and their clear intersection, the idea that they could work in favor of recrystallization by the TDRX mechanism was fortified [44]. In addition to the nucleation and growth as that happened during DDRX (Fig. 5(a)), they were convinced that the formation of the new grains could occur through the gradual transformation of low-angle boundaries to high-angle ones by the absorption of more dislocations with the increase in the applied strain. This process could also accomplish the nucleation by TDRX mechanism, as discussed before. The CDRX was intrinsically a gradual process with strain and it took part in grain refinement by increase in the ECAP pass number [55]. Eventually, the primary grains were transformed to finer grains during the successive passes, but no change occurred in the primary dynamic recrystallized grains.

Fig. 6 displays the trend of grain size reduction after one, two, and three passes of AEB. As seen, the average grain size gradually decreased from about
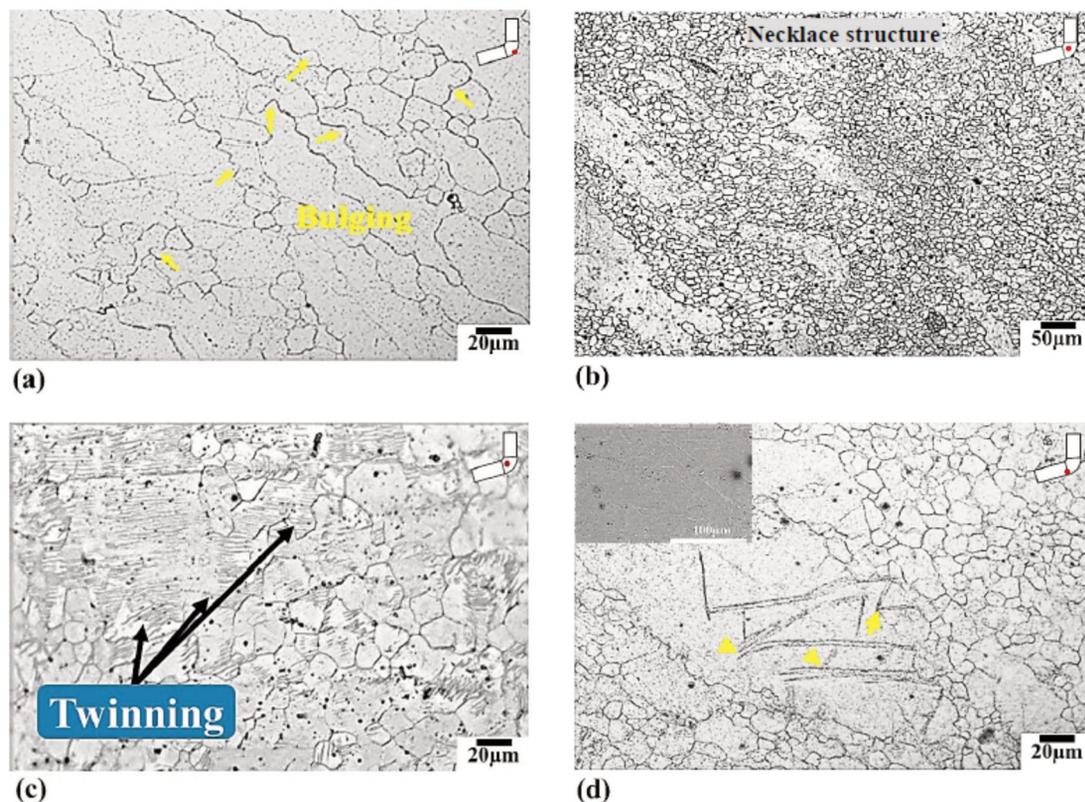
Figure 5. *Optical micrographs showing the (a) the grain boundary bulging in the lower part of ECAP region, (b) the necklace structure in the middle of ECAP region, (c) the formation of twin boundaries and their role on the recrystallization of Mg-0.8Mn-0.5Ca after one-pass of AEB and (d) in the middle and after of ECAP region, respectively (the inset in (d) shows the SEM image of twin boundaries in the ECAP region)*

448 μm in the homogenized sample (Fig. 6(a)) to 49, 12.5, and 1.5 μm after the first, second ,and third pass of AEB (Figs. 6(b-d)). The gradual decrease in the surface fraction of recrystallized regions and average grain size strengthened the idea that CDRX played a major role in the recrystallization behavior of AEBed Mg-0.8Mn-0.5Ca.

3.3. Mechanical properties

Fig. 7 exhibits the tensile and compressive stress-strain curves of the homogenized and AEBed samples. It is evident that by increasing the passes number, the compressive and tensile strengths improved, while the compressive and tensile elongations decreased. The tensile and compressive strengths of the homogenized alloy were 150 and 205 MPa, respectively. After the third pass, the tensile and compressive strengths enhanced to 330 and 301 MPa that represent 2 and 1.5 times increase, respectively (Table 2). The strength improvement could be attributed to the considerable grain refinement observed in Fig. 6 [56-58]. As mentioned before, the average grain size of the homogenized sample and after three passes of ABE was 448 μm and 1.5 μm, respectively.

The results also showed that the elongation of processed samples decreased as their strength rose with increased pass number (Table 2). The reduction in elongation was partly ascribed to the heavily work hardened microstructure, the large amount of non-uniform strains induced during process, and inhomogeneous microstructure [59, 60]. The considerable increase in the number of dislocations increased their interactions and formed a lot of dislocation tangles. The density of dislocations and dislocation tangles increasingly increased with the effective strain and passes number. Hence, the decreased elongation in AEBed samples was related to the short mean-free path of dislocations in the highly work hardened matrix [46].

Fig. 8 shows the SEM micrographs from the fractured surface of tensile samples. As shown in Fig. 8(a), the homogenized sample showed a typical ductile fracture with deep dimples. The ductile fracture began with the nucleation of dimples at locations with stress concentration or around inclusions [61]. Afterwards, the dimples grew and coalesced to form micro-cracks. The growth of micro-cracks and cutting the cross-section were the next steps. Finally, the metal-to-metal contact area became too small to support the load and fracture occurred. After one-pass of AEB the fracture surface showed refined dimples (Fig. 8(b)). Finer dimples in one-pass
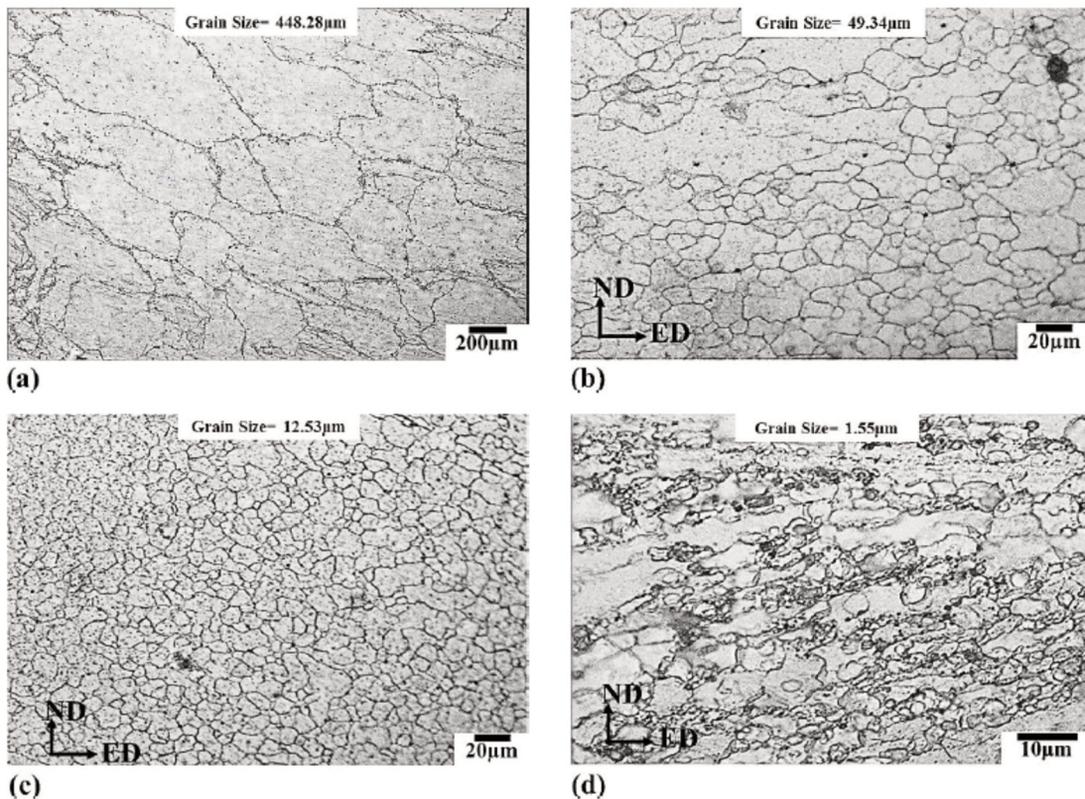
***Figure 6.** Optical micrographs of the samples at different conditions; (a) homogenized, (b) after the first pass, (c) after the second pass and (d) after the third pass ABE process*
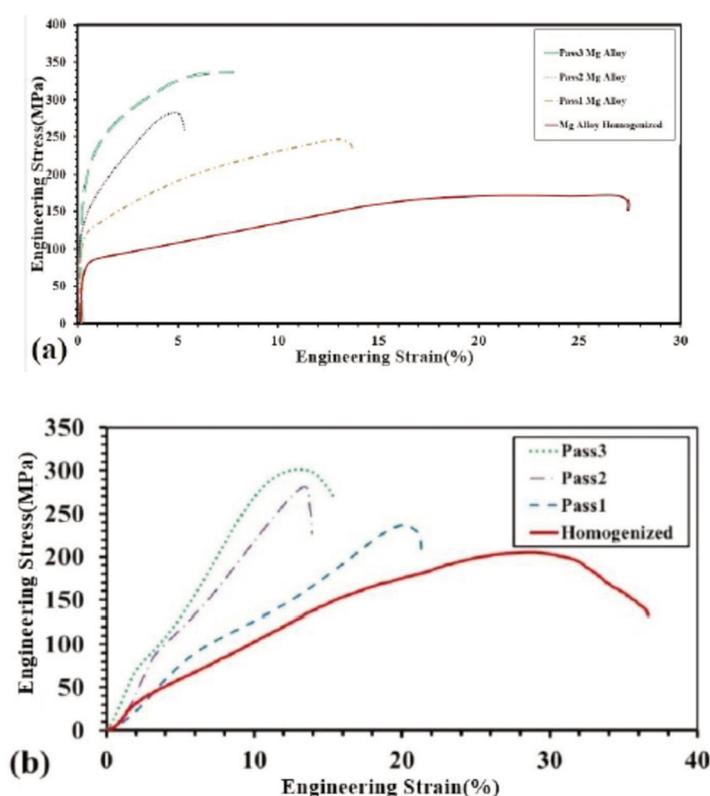
Figure 7. *Tensile (a) and compressive stress-strain (b) curves of the homogenized and AEBed samples*

Table 2. *Mechanical characteristics of the investigated Mg-Mn-Ca alloy at different conditions*

Sample	Compression properties			Tensile properties		
	YS (MPa)	UTS (MPa)	Failure strain (%)	YS (MPa)	UTS (MPa)	Failure strain (%)
Homogenized	50	205	36.2	60	150	28
1-pass ABE	70	240	20.5	105	240	14
2-pass ABE	115	280	12	130	275	5.5
3-pass ABE	140	301	15.6	176	330	8

processed samples was consistent with its lower ductility. This was because the size of dimples was an index to the level of ductility, so that the larger dimples, the higher ductility would be. Hence, comparison of dimples size in Figs. 8(a) and 8(b) implied that ductility decreased after one pass of AEB. Fig. 8(c and d) shows that after the second and third passes dimples size became finer and elongated dimples were observed. The shallow and narrow elongated dimples indicated that the failure mode changed to shear ductile rupture. In addition, the appearance of shear lips and facets, shown by arrows, implied that a combined mode of ductile-cleavage governed the fracture morphology of 2-pass and 3-pass processed samples. These observations well

agree with the reduced elongation in Fig. 7.

3.4. Biocorrosion behavior

Fig. 9(a) demonstrates the potentio-dynamic polarization (PDP) curves of the homogenized specimen and the samples processed by one, two, and three AEB passes in the SBF solution. In the early stages of the test, the anodic polarization curves showed a high corrosion rate. By reaching the passive region, the anodic polarization curves were stabilized. The passive region of the anodic polarization curves may be related to the formation of corrosion products that acted as the protective coating on the material surface [6, 7]. As shown in Fig. 9(a), by increase in
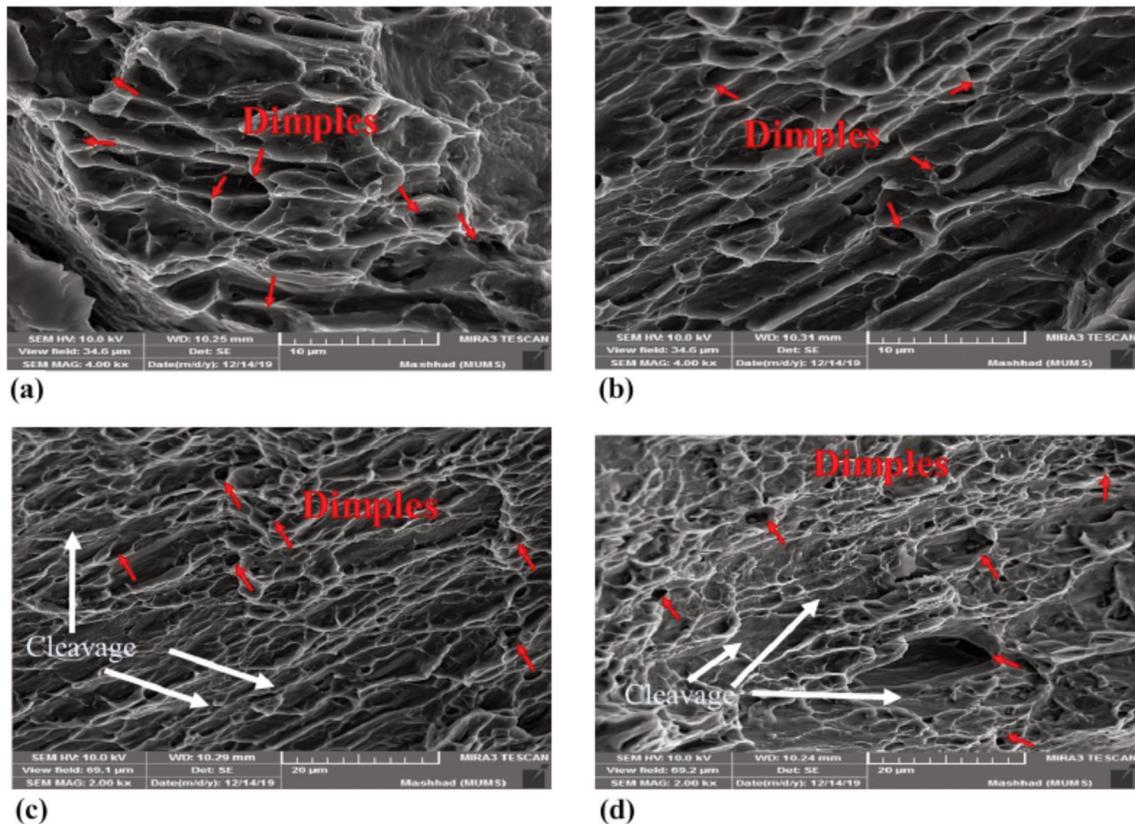
Figure 8. SEM micrographs showing the fractured surfaces of the samples at different conditions of (a) homogenized, (b) 1-pass, (c) 2-pass and (d) 3-pass ABE process

the number of AEB passes, the rate of anodic and cathodic reactions declined, so that the curves were shifted to the upper left side.

Table 3 reports electrochemical parameters of different samples in SBF solution. The current density of the homogenized sample was 63 $\mu A/Cm^2$, which was much higher than that of the three passes processed sample (3.63 $\mu A/Cm^2$). Based on the Eq. (3), the corrosion rate decreased from 1.439 for homogenized sample to 0.082 mm/year for 3-pass ABEed sample and the corrosion resistance (R_p in Eq. (4)) improved from 1.1 kΩ for the homogenized sample to 14.159 kΩ for the 3-pass processed sample.

By increase in the number of passes, the current density and electrochemical potential decreased, which indicated the material became nobler (reducing the corrosion rate). This improvement could be related to the corresponding changes in the grain size of material by AEB. By increasing the number of the passes of the process, the grain size decreased and this structural modification enhanced the corrosion resistance. Improvement of corrosion resistance by the decrease in the grain size could be attributed to (1) the decrease in the volume increase-induced stresses as a result of lower damage of protective layer and (2)

formation of more adhesive and strong protective layer on the sample surface [25, 60]. However, in the ABEed samples, the formation of the hydroxyapatite (HA) protective layer on the surface of the Mg-Mn-Ca alloy caused a significant improvement of the corrosion resistance.

During the HEI test the following reaction happened [19]:

$$Mg + 2H_2O \rightarrow Mg\left(OH\right)_2 + H_2 \qquad (11)$$

Fig. 9(b) exhibits the HE tests results of different samples immersed in SBF solution for 168 h. The aggregation of corrosion products on the surface gradually reduced the rate of HE. The volume of generated hydrogen increased with the increase in the immersion time. This was attributed to the destruction of the corrosion products and penetration of the corrosive solution to the surface underneath. The results implied that by increasing the number of AEB passes, the volume of generated hydrogen declined.

The morphology of corroded surface and the composition of the corrosion products of different samples, immersed in SBF solution for 7 days were investigated by FESEM (Fig. 9(c-e)). As shown in
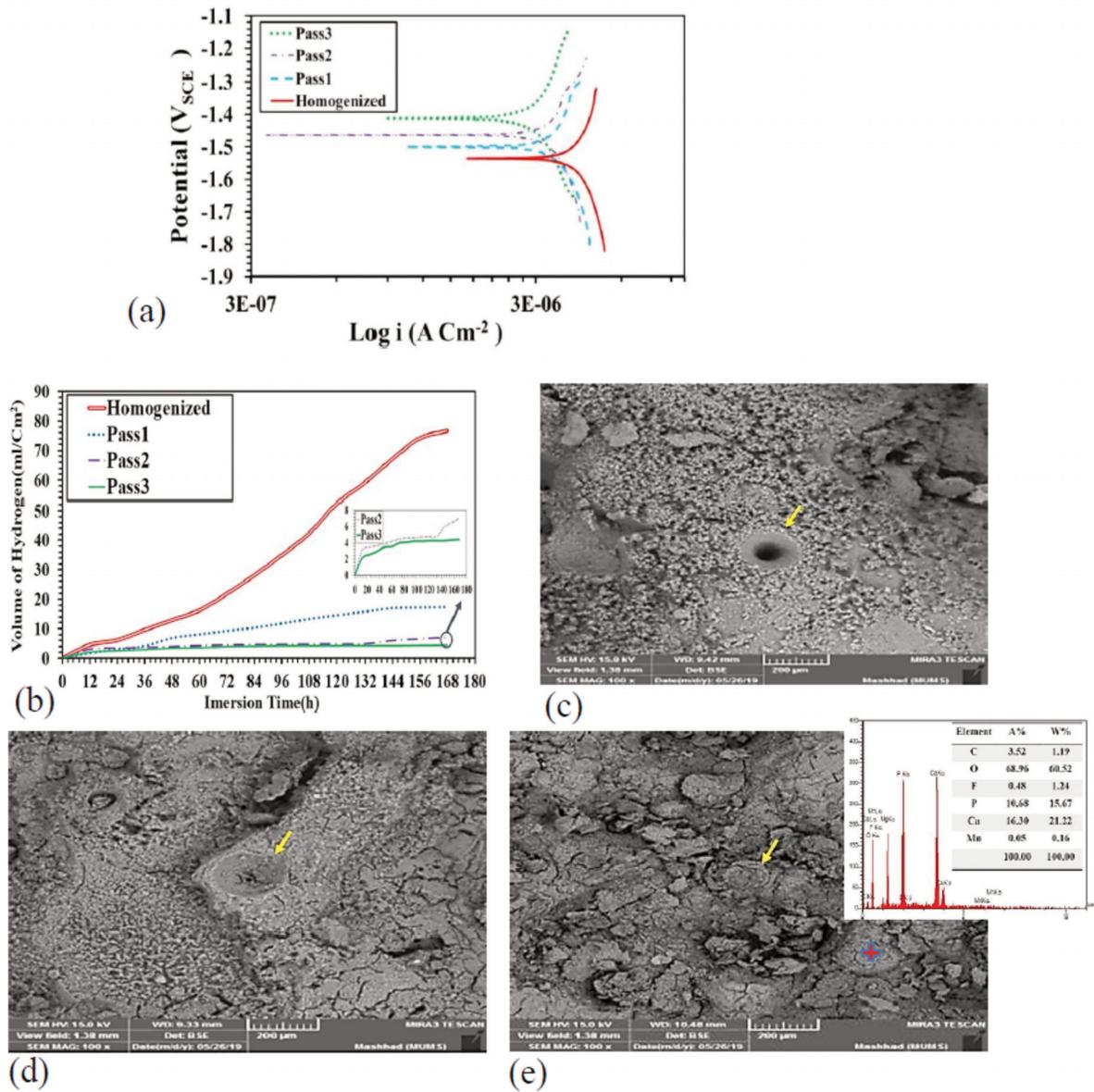
Figure 9. *(a) PDP test diagrams, (b) hydrogen evolution diagrams, FESEM micrographs from the samples subjected to HE test at different conditions of (c) homogenized, (d) 1-pass and (e) 3-pass ABE process*

Table 3. *Electrochemical parameters of different samples in SBF solution*

Sample	Corrosion potential $E_{Corr}(mV_{SCE})$	Current density $i_{Corr}\left(\dfrac{\mu A}{Cm^2}\right)$	Cathodic slope $\beta_c\left(\dfrac{mV}{Dec_{SCE}}\right)$	Anodic slope $\beta_a\left(\dfrac{mV}{Dec_{SCE}}\right)$	Polarization resistance $R_p\left(K\Omega Cm^2\right)$	Corrosion rate $P_i\left(\dfrac{mm}{year}\right)$
Mg Alloy Homogenized	-1.533	63	0.378	0.274	1.1	14.395
1-pass ABE	-15.012	13.20	0.253	0.258	4.234	0.3016
3-pass ABE	-1.415	36.308	0.257	0.219	14.159	0.08296

Fig. 9(c), severe homogeneous corrosion occurred in the homogenized sample. The corroded surface could be divided into two zones, suggesting various corrosion mechanisms. The first zones were deep pits indicating the severe pitting corrosion. Lack of corrosion products around the pits indicated that they acted as the deep channels for the penetration of solution to the surface. The second zones were smooth and low corroded areas with a network-like morphology. Comparing the SEM micrographs helped to deduce that the depth of corrosion pits was much smaller in AEBed samples than in the homogenized sample. Also, the dense layer of hydroxyapatite in fine-grained (especially 2-pass and 3-pass processed) samples seemed to be responsible for slowing down the HE (Fig. 9(e)). For the homogenized microstructure, the corrosion product layer was loose which was easily formed in vicinity of grain boundaries. Generally, the high density of grain boundaries was associated with the change of the structure discontinuity between the Mg matrix and layer, which was beneficial for the formation of dense product layer [50, 62]. The precipitated network-like film on the surface of the AEBed samples had calcium phosphate compounds such as hydroxyapatite, which were formed due to the reaction of phosphate and calcium ions with hydroxide ions in the SBF solution. In addition, the pits in AEBed samples were covered with corrosion products. The corroded surface of AEBed samples contained numerous micro-cracks, which were nearly absent on the surface of the homogenized sample.

Table 4 compares the corrosion rate of the Mg-0.8Mn-0.5Ca alloy processed by ABE with other results reported in literature, which indicated a considerable improvement in corrosion resistance in the processed samples in the present work.

4. Conclusions

In this study, the effect of 1-3 passes of accumulative extrusion bonding (AEB) through 120°-angle channels at 400 °C on the microstructure, mechanical properties, and biocorrosion behavior of Mg-0.8Mn-0.5Ca (wt. %) alloy was investigated. The major conclusions can be summarized as follows:

The simulation of AEB process showed that the average effective plastic strain per pass for channels with the internal angle of 120° was about 1.93. This value was nearly 2 times of the average effective plastic strain reported for one pass of conventional ECAP.

The average grain size was dramatically decreased from about 448.3 μm for the homogenized (starting) alloy to 1.55 μm for the three passes of deformation. Microstructural observations suggested a combination of continuous, discontinuous, and twinning-induced dynamic recrystallization as the major mechanisms responsible for the observed grain refinement.

Tensile and compressive strengths after three passes of AEB showed 2 and 1.5 times improvements due to considerable decrease in the average grain size, respectively.

Tensile elongation decreased from 26 % for the homogenized sample to 7.5 % after three passes of ABE process due to the severe work-hardening, non-uniform strain, and inhomogenies microstructure.

Corrosion resistance increased from 1.1 to 14.159 after three passes of ABE. Grain refinement by AEB resulted in the formation of hydroxyapatite layer with a more uniform distribution on the grain boundaries. The hydroxyapatite layer imparted better corrosion resistance to the AEBed samples.

Table 4. Comparison of the lowest corrosion rate of the Mg-0.8Zn-0.5Ca alloy processed by ABE with reported values for different alloys in the literature

Alloy	State	Solution	Corrosion rate (mm/y)	Ref
Mg-2Zn-Ca-0.5Mn	As-cast	Hank's	1.58	[63]
Mg-2Zn-Ca-0.5Mn-1.3Ce	As-cast	Hank's	1.34	[63]
Mg–2Ca–0.5Mn–2Zn	As-cast	SBF	1.78	[4]
Mg–2Ca–0.5Mn–4Zn	As-cast	SBF	2.27	[4]
Mg–2Ca–0.5Mn–7Zn	As-cast	SBF	3.98	[4]
Mg-Zn-1.5-Ca-1.1Mn	As-cast	Hank's	1.40	[64]
6h-coated Mg-2Zn-Ca-0.5Mn-1.3Ce	As-cast	Hank's	1.29	[65]
ZK60	As-extruded	Hank's	0.32	[66]
Annealed Mg-Zn-Ca	SPD (HPT)	SBF	1.30	[62]
Mg-0.8Mn-0.5Ca	ABE	SBF	0.08	Present work

Author`s Contribution

This paper was extracted from PhD thesis of Mr. M. Khani under supervision of Dr. G.R. Ebrahimi and counselors of Dr. H.R. Ezatpour and Dr. A. Momeni.

Conflict of interest

The authors declare that there is no conflict of interest.

Data availability

The authors confirm that the data supporting the findings of this study are available within the article and/or its supplementary materials.

References

[1] N. Li, Y. Zheng, Novel magnesium alloys developed for biomedical application: A Review, Journal of Materials Science & Technology, 29 (6) (2013) 489-502. https://doi.org/10.1016/j.jmst.2013.02.005

[2] S. Hiromoto, T. Shishido, A. Yamamoto, N. Maruyama, H. Somekawa, T. Mukai, Precipitation control of calcium phosphate on pure magnesium by anodization, Corrosion Science, 50 (10) (2008) 2906-2913. https://doi.org/10.1016/j.corsci.2008.08.013

[3] S. Ramezanzade, G. R. Ebrahimi, M. Torabi Parizi, H. R. Ezatpour. Synergetic effect of GNPs and MgOs on the mechanical properties of Mg–Sr–Ca alloy, Materials Science and Engineering: A, 761 (2019) 138025. https://doi.org/10.1016/j.msea.2019.138025

[4] H.R. Bakhsheshi-Rad, M.H. Idris, M.R. Abdul-Kadir, A. Ourdjini, M. Medraj, M. Daroonparvar, E. Hamzah, Mechanical and bio-corrosion properties of quaternary Mg-Ca-Mn-Zn alloys compared with binary Mg-Ca alloys, Materials and Design, 53 (2014) 283-292. https://doi.org/10.1016/j.matdes.2013.06.055

[5] R. Lapovok, P.F. Thomson, R. Cottam, Y. Estrin, The effect of grain refinement by warm equal channel angular extrusion on room temperature twinning in magnesium alloy ZK60, Journal of Materials Science, 40 (7) (2005) 1699-1708. https://doi.org/10.1007/s10853-005-0672-1

[6] H. Miura, T. Maruoka, X. Yang, J.J. Jonas, Microstructure and mechanical properties of multi-directionally forged Mg-Al-Zn alloy, Scripta Materialia, 66 (1) (2012) 49-51. https://doi.org/10.1016/j.scriptamat.2011.10.005

[7] R.B. Figueiredo, T.G. Langdon, Grain refinement and mechanical behavior of a magnesium alloy processed by ECAP, Journal of Materials Science, 45 (17) (2010) 4827-4836. https://doi.org/10.1007/s10853-010-4589-y

[8] S. Kaabi Falahieh Asl, S. Nemeth, M.J. Tan, Hydrothermally deposited protective and bioactive coating for magnesium alloys for implant application, Surface and Coatings Technology, 258 (2014) 931-937. https://doi.org/10.1016/j.surfcoat.2014.07.055

[9] X.N. Gu, N. Li, W.R. Zhou, Y.F. Zheng, X. Zhao, Q.Z. Cai, L. Ruan, Corrosion resistance and surface biocompatibility of a microarc oxidation coating on a Mg-Ca alloy, Acta Biomaterialia, 7 (4) (2011) 1880-1889. https://doi.org/10.1016/j.actbio.2010.11.034

[10] H.X. Wang, S.K. Guan, X. Wang, C.X. Ren, L.G. Wang, In vitro degradation and mechanical integrity of Mg–Zn–Ca alloy coated with Ca-deficient hydroxyapatite by the pulse electrodeposition process, Acta Biomaterialia, 6 (5) (2010) 1743-1748. https://doi.org/10.1016/j.actbio.2009.12.009

[11] S. Agarwal, J. Curtin, B. Duffy, S. Jaiswal, Biodegradable magnesium alloys for orthopaedic applications: A review on corrosion, biocompatibility and surface modifications, Materials Science and Engineering: C, 68 (2016) 948-963. https://doi.org/10.1016/j.msec.2016.06.020

[12] J. Fan, X. Qiu, X. Niu, Z. Tian, W. Sun, X. Liu, Y. Li, W. Li, J. Meng, Microstructure, mechanical properties, in vitro degradation and cytotoxicity evaluations of Mg–1.5Y–1.2Zn–0.44Zr alloys for biodegradable metallic implants, Materials Science and Engineering: C, 33 (4) (2013) 2345-2352. https://doi.org/10.1016/j.msec.2013.01.063

[13] T. Lei, W. Tang, S.-H. Cai, F.-F. Feng, N.-F. Li, On the corrosion behaviour of newly developed biodegradable Mg-based metal matrix composites produced by in situ reaction, Corrosion Science, 54 (2012) 270-277. https://doi.org/10.1016/j.corsci.2011.09.027

[14] M.C. Turhan, Q. Li, H. Jha, R.F. Singer, S. Virtanen, Corrosion behaviour of multiwall carbon nanotube/magnesium composites in 3.5% NaCl, Electrochimica Acta, 56 (20) (2011) 7141-7148. https://doi.org/10.1016/j.electacta.2011.05.082

[15] E.C. Meng, S.K. Guan, H.X. Wang, L.G. Wang, S.J. Zhu, J.H. Hu, C.X. Ren, J.H. Gao, Y.S. Feng, Effect of electrodeposition modes on surface characteristics and corrosion properties of fluorine-doped hydroxyapatite coatings on Mg–Zn–Ca alloy, Applied Surface Science, 257 (11) (2011) 4811-4816. https://doi.org/10.1016/j.apsusc.2010.12.073

[16] D. Orlov, G. Raab, T.T. Lamark, M. Popov, Y. Estrin, Improvement of mechanical properties of magnesium alloy ZK60 by integrated extrusion and equal channel angular pressing, Acta Materialia, 59 (1) (2011) 375-385. https://doi.org/10.1016/j.actamat.2010.09.043

[17] X.N. Gu, Y.F. Zheng, Y. Cheng, S.P. Zhong, T.F. Xi, In vitro corrosion and biocompatibility of binary magnesium alloys, Biomaterials, 30 (4) (2009) 484-498. https://doi.org/10.1016/j.biomaterials.2008.10.021

[18] R. Radha, D. Sreekanth, Insight of magnesium alloys and composites for orthopedic implant applications – a review, Journal of Magnesium and Alloys, 5 (3) (2017) 286-312. https://doi.org/10.1016/j.jma.2017.08.003

[19] M. Kaviani, G.R. Ebrahimi, H.R. Ezatpour, Improving the mechanical properties and biocorrosion resistance of extruded Mg-Zn-Ca-Mn alloy through hot deformation, Materials Chemistry and Physics, 234 (2019) 245-258. https://doi.org/10.1016/j.matchemphys.2019.06.010

[20] B.S. Padekar, R.K. Singh Raman, V.S. Raja, L. Paul, Stress corrosion cracking of a recent rare-earth containing magnesium alloy, EV31A, and a common Al-containing alloy, AZ91E, Corrosion Science, 71 (2013) 1-9.

https://doi.org/10.1016/j.corsci.2013.01.001

[21] H.-Y. Ha, H.J. Kim, S.-M. Baek, B. Kim, S.-D. Sohn, H.-J. Shin, H.Y. Jeong, S.H. Park, C.D. Yim, B.S. You, J.G. Lee, S.S. Park, Improved corrosion resistance of extruded Mg–8Sn–1Zn–1Al alloy by microalloying with Mn, Scripta Materialia, 109 (2015) 38-43. https://doi.org/10.1016/j.scriptamat.2015.07.013

[22] Y. Ding, C. Wen, P. Hodgson, Y. Li, Effects of alloying elements on the corrosion behavior and biocompatibility of biodegradable magnesium alloys: a review, Journal of Materials Chemistry B, 2 (14) (2014) 1912-1933. https://doi.org/10.1039/C3TB21746A

[23] Y. Ali, D. Qiu, B. Jiang, F. Pan, M.-X. Zhang, Current research progress in grain refinement of cast magnesium alloys: A review article, Journal of Alloys and Compounds, 619 (2015) 639-651. https://doi.org/10.1016/j.jallcom.2014.09.061

[24] F. Zhang, A. Ma, D. Song, J. Jiang, F. Lu, L. Zhang, D. Yang, J. Chen, Improving in-vitro biocorrosion resistance of Mg-Zn-Mn-Ca alloy in Hank's solution through addition of cerium, Journal of Rare Earths, 33 (1) (2015) 93-101. https://doi.org/10.1016/S1002-0721(14)60388-4

[25] S.Z. Khalajabadi, N. Ahmad, A. Yahya, M.A.M. Yajid, A. Samavati, S. Asadi, A. Arafat, M.R. Abdul Kadir, The role of titania on the microstructure, biocorrosion and mechanical properties of Mg/HA-based nanocomposites for potential application in bone repair, Ceramics International, 42 (16) (2016) 18223-18237. https://doi.org/10.1016/j.ceramint.2016.08.146

[26] X. Wang, P. Zhang, L.H. Dong, X.L. Ma, J.T. Li, Y.F. Zheng, Microstructure and characteristics of interpenetrating β-TCP/Mg–Zn–Mn composite fabricated by suction casting, Materials & Design (1980-2015), 54 (2014) 995-1001. https://doi.org/10.1016/j.matdes.2013.09.037

[27] M. Razavi, M.H. Fathi, M. Meratian, Bio-corrosion behavior of magnesium-fluorapatite nanocomposite for biomedical applications, Materials Letters, 64 (22) (2010) 2487-2490. https://doi.org/10.1016/j.matlet.2010.07.079

[28] H. Wang, S. Guan, Y. Wang, H. Liu, H. Wang, L. Wang, C. Ren, S. Zhu, K. Chen, In vivo degradation behavior of Ca-deficient hydroxyapatite coated Mg–Zn–Ca alloy for bone implant application, Colloids and Surfaces B: Biointerfaces, 88 (1) (2011) 254-259. https://doi.org/10.1016/j.colsurfb.2011.06.040

[29] M. Li, Y. Cheng, Y.F. Zheng, X. Zhang, T.F. Xi, S.C. Wei, Plasma enhanced chemical vapor deposited silicon coatings on Mg alloy for biomedical application, Surface and Coatings Technology, 228 (2013) S262-S265. https://doi.org/10.1016/j.surfcoat.2012.05.128

[30] E.C. Meng, S.K. Guan, H.X. Wang, L.G. Wang, S.J. Zhu, J.H. Hu, C.X. Ren, J.H. Gao, Y.S. Feng, Effect of electrodeposition modes on surface characteristics and corrosion properties of fluorine-doped hydroxyapatite coatings on Mg-Zn-Ca alloy, Applied Surface Science, 257 (11) (2011) 4811-4816. https://doi.org/10.1016/j.apsusc.2010.12.073

[31] R. del Campo, B. Savoini, A. Muñoz, M.A. Monge, R. Pareja, Processing and mechanical characteristics of magnesium-hydroxyapatite metal matrix biocomposites, Journal of the Mechanical Behavior of Biomedical Materials, 69 (2017) 135-143. https://doi.org/10.1016/j.jmbbm.2016.12.023

[32] Y. Huang, D. Liu, L. Anguilano, C. You, M. Chen, Fabrication and characterization of a biodegradable Mg–2Zn–0.5Ca/1β-TCP composite, Materials Science and Engineering: C, 54 (2015) 120-132. https://doi.org/10.1016/j.msec.2015.05.035

[33] K.B. Nie, K.K. Deng, X.J. Wang, T. Wang, K. Wu, Influence of SiC nanoparticles addition on the microstructural evolution and mechanical properties of AZ91 alloy during isothermal multidirectional forging, Materials Characterization, 124 (2017) 14-24. https://doi.org/10.1016/j.matchar.2016.12.006

[34] S. Rusz, O. Hilšer, V. Ochodek, L. Čížek, M. Kraus, V. Mareš, A. Grajcar, J. Švec, Effect of severe plastic deformation on mechanical and fatigue behaviour of medium-c sheet steel, Journal of Mining and Metallurgy, Section B: Metallurgy, 56 (2) (2020) 161-170. https://doi.org/10.2298/JMMB190910008R

[35] G.K. Manjunath, K. Udaya Bhat, G.V. Preetham Kumar, M.R. Ramesh, Microstructure and wear performance of ECAP processed cast Al–Zn–Mg alloys, Transactions of the Indian Institute of Metals, 71 (8) (2018) 1919-1931. https://doi.org/10.1007/s12666-018-1328-6

[36] H.K. Kim, The grain size dependence of flow stress in an ECAPed AZ31 Mg alloy with a constant texture, Materials Science and Engineering A, 515 (1-2) (2009) 66-70. https://doi.org/10.1016/j.msea.2009.02.039

[37] S.M. Masoudpanah, R. Mahmudi, The microstructure, tensile, and shear deformation behavior of an AZ31 magnesium alloy after extrusion and equal channel angular pressing, Materials & Design, 31 (7) (2010) 3512-3517. https://doi.org/10.1016/j.matdes.2010.02.018

[38] P. Bernard, S. Bag, K. Huang, R.E. Logé, A two-site mean field model of discontinuous dynamic recrystallization, Materials Science and Engineering A, 528 (24) (2011) 7357-7367. https://doi.org/10.1016/j.msea.2011.06.023

[39] D.G. Cram, H.S. Zurob, Y.J.M. Brechet, C.R. Hutchinson, Modelling discontinuous dynamic recrystallization using a physically based model for nucleation, Acta Materialia, 57 (17) (2009) 5218-5228. https://doi.org/10.1016/j.actamat.2009.07.024

[40] F. Montheillet, O. Lurdos, G. Damamme, A grain scale approach for modeling steady-state discontinuous dynamic recrystallization, Acta Materialia, 57 (5) (2009) 1602-1612. https://doi.org/10.1016/j.actamat.2008.11.044

[41] F.J. Humphreys, M. Hotherly, Recrystallization and Related Annealing Phenomena, Second Edition, Oxford, Pergamon Press, New York, 2004, pp.252. (9780080982694)

[42] A. Yamashita, Z. Horita, T.G. Langdon, Improving the mechanical properties of magnesium and a magnesium alloy through severe plastic deformation, Materials Science and Engineering: A, 300 (1) (2001) 142-147. https://doi.org/10.1016/S0921-5093(00)01660-9

[43] M. Kavyani, G.R. Ebrahimi, H.R. Ezatpour, M. Jahazi, Microstructure refinement, mechanical and biocorrosion properties of Mg–Zn–Ca–Mn alloy improved by a new severe plastic deformation process, Journal of Magnesium and Alloys, (2021)

https://doi.org/10.1016/j.jma.2020.11.013

[44] Q. Ma, B. Li, E.B. Marin, S.J. Horstemeyer, Twinning-induced dynamic recrystallization in a magnesium alloy extruded at 450 °C, Scripta Materialia, 65 (9) (2011) 823-826.
https://doi.org/10.1016/j.scriptamat.2011.07.046

[45] P. C. Wu, C. P. Chang, P. W. Kao, The distribution of dislocation walls in the early processing stage of equal channel angular extrusion, Materials Science and Engineering A, 374 (1-2) (2004) 196-203.
https://doi.org/10.1016/j.msea.2004.02.016

[46] G. A. Malygin, Mechanism of strain hardening and dislocation-structure formation in metals subjected to severe plastic deformation, Physics of the Solid State, 48 (4) (2006) 693-699.
https://doi.org/10.1134/S1063783406040123

[47] X. Luo, Z. Feng, T. Yu, T. Huang, R. Li, G. Wu, N. Hansen, X. Huang, Microstructural evolution in Mg-3Gd during accumulative roll-bonding, Materials Science and Engineering A, 772 (2020) 138763.
https://doi.org/10.1016/j.msea.2019.138763

[48] L. Hou, T. Wang, R. Wu, J. Zhang, M. Zhang, A. Dong, B. Sun, S. Betsofen, B. Krit, Microstructure and mechanical properties of Mg-5Li-1Al sheets prepared by accumulative roll bonding, Journal of Materials Science and Technology, 34 (2) (2018) 317-323.
https://doi.org/10.1016/j.jmst.2017.02.005

[49] S. Amirkhanlou, M. Ketabchi, N. Parvin, S. Khorsand, R. Bahrami, Accumulative press bonding; a novel manufacturing process of nanostructured metal matrix composites, Materials & Design, 51 (2013) 367-374.
https://doi.org/10.1016/j.matdes.2013.04.032

[50] E.A. El-Danaf, M.S. Soliman, A.A. Almajid, M.M. El-Rayes, Enhancement of mechanical properties and grain size refinement of commercial purity aluminum 1050 processed by ECAP, Materials Science and Engineering: A, 458 (1) (2007) 226-234.
https://doi.org/10.1016/j.msea.2006.12.077

[51] L. Olejnik, A. Rosochowski, Methods of fabricating metals for nano-technology, Bulletin of the Polish Academy of Sciences: Technical Sciences, 53 (4) (2005) 413-423.

[52] M. Eizadjou, H. Danesh Manesh, K. Janghorban, Mechanism of warm and cold roll bonding of aluminum alloy strips, Materials & Design, 30 (10) (2009) 4156-4161.
https://doi.org/10.1016/j.matdes.2009.04.036

[53] R. B. Figueiredo, T.G. Langdon, Principles of grain refinement and superplastic flow in magnesium alloys processed by ECAP, Materials Science and Engineering: A, 501 (1) (2009) 105-114.
https://doi.org/10.1016/j.msea.2008.09.058

[54] K. Máthis, J. Gubicza, N.H. Nam, Microstructure and mechanical behavior of AZ91 Mg alloy processed by equal channel angular pressing, Journal of Alloys and Compounds, 394 (1) (2005) 194-199.
https://doi.org/10.1016/j.jallcom.2004.10.050

[55] P. Klimanek, A. Pötzsch, Microstructure evolution under compressive plastic deformation of magnesium at different temperatures and strain rates, Materials Science and Engineering: A, 324 (1) (2002) 145-150.
https://doi.org/10.1016/S0921-5093(01)01297-7

[56] C. W. Su, L. Lu, M. O. Lai, A model for the grain refinement mechanism in equal channel angular pressing of Mg alloy from microstructural studies, Materials Science and Engineering: A, 434 (1) (2006). 227-236. https://doi.org/10.1016/j.msea.2006.06.103

[57] L. Jin, D. Lin, D. Mao, X. Zeng, B. Chen, W. Ding, Microstructure evolution of AZ31 Mg alloy during equal channel angular extrusion, Materials Science and Engineering A, 423 (1-2) (2006) 247-252.
https://doi.org/10.1016/j.msea.2006.02.045

[58] F. Witte, F. Feyerabend, P. Maier, J. Fischer, M. Störmer, C. Blawert, W. Dietzel, N. Hort, Biodegradable magnesium–hydroxyapatite metal matrix composites, Biomaterials, 28 (13) (2007) 2163-2174.
https://doi.org/10.1016/j.biomaterials.2006.12.027

[59] X. Zhang, G. Yuan, J. Niu, P. Fu, W. Ding, Microstructure, mechanical properties, biocorrosion behavior, and cytotoxicity of as-extruded Mg-Nd-Zn-Zr alloy with different extrusion ratios, Journal of the Mechanical Behavior of Biomedical Materials, 9 (2012) 153-162.
https://doi.org/10.1016/j.jmbbm.2012.02.002

[60] L. B. Tong, J. H. Chu, W.T. Sun, Z.H. Jiang, D.N. Zou, K.S. Wang, S. Kamado, M.Y. Zheng, Development of high-performance Mg–Zn–Ca–Mn alloy via an extrusion process at relatively low temperature, Journal of Alloys and Compounds, 825 (2020).
https://doi.org/10.1016/j.jallcom.2020.153942

[61] H. R. Ezatpour, S. A. Sajjadi, M. H. Sabzevar, Y. Z. Huang, An investigation of the tensile and compressive properties of Al6061 and its nanocomposites in as-cast state and in extruded condition, Materials Science and Engineering: A, 607 (2014) 589-595.
https://doi.org/10.1016/j.msea.2014.04.036

[62] C. Zhang, S. Guan, L. Wang, S. Zhu, L. Chang, The microstructure and corrosion resistance of biological Mg–Zn–Ca alloy processed by high-pressure torsion and subsequently annealing, Journal of Materials Research, 32 (6) (2017) 1061-1072.
https://doi.org/10.1557/jmr.2017.55

[63] F. Zhang, M. Aibin, S. Dan, J. Jiang, L. Fumin, L. Zhang. Improving in-vitro biocorrosion resistance of Mg-Zn-Mn-Ca alloy in Hank's solution through addition of cerium, Journal of Rare Earths, 33 (2015) 93-101. https://doi.org/10.1016/S1002-0721(14)60388-4

[64] X. Zhang, Z. Wang, G. Yuan, Y. Xue, Improvement of mechanical properties and corrosion resistance of biodegradable Mg–Nd–Zn–Zr alloys by double extrusion, Materials Science and Engineering: B, 177 (13) (2012) 1113-1119.
https://doi.org/10.1016/j.mseb.2012.05.020

[65] D. Song, G. Guo, J. Jiang, L. Zhang, A. Ma, X. Ma, J. Chen, Z. Cheng, Hydrothermal synthesis and corrosion behavior of the protective coating on Mg-2Zn-Mn-Ca-Ce alloy, Progress in Natural Science: Materials International, 26 (6) (2016) 590-599.
https://doi.org/10.1016/j.pnsc.2016.11.002

[66] X. Lin, L. Tan, Q. Zhang, K. Yang, Z. Hu, J. Qiu, Y. Cai, The in vitro degradation process and biocompatibility of a ZK60 magnesium alloy with a forsterite-containing micro-arc oxidation coating, Acta Biomaterialia, 9 (10) (2013) 8631-8642.
https://doi.org/10.1016/j.actbio.2012.12.016

UTICAJ NOVE INTENZIVNE PLASTIČNE DEFORMACIJE NA MIKROSTRUKTURU, MEHANIČKA I KOROZIVNA SVOJSTVA Mg-0.8Mn-0.5Ca LEGURE

M. Khani [a], G.R. Ebrahimi [b, *], H.R. Ezatpour [c], A. Momeni [d]

[a] Odsek za inženjerstvo materijala i polimera, Univerzitet Hakima Sabzevarija, Sabzevar, Iran
[b] Odsek za materijale i metalurško inženjerstvo, Fakultet inženjerskih nauka, Univerzitet Ferdovsi u Mašhadu, Mašhad, Iran
[c] Odsek za inženjerske nauke, Univerzitet Hakima Sabzevarija, Sabzevar, Iran
[d] Odsek za nauku o materijalima i inženjerstvo, Tehnološki univerzitet u Hamadanu, Hamadan, Iran

Apstrakt

U ovom radu je ispitivan uticaj akumulativnog spajanja ekstruzijom na mikrostrukturu i mehanička svojstva biokompatibilne Mg-0.8Mn-0.5Ca legure. Cilj ovog istraživanja bio je da se razviju mehanička i korozivna svojstva Mg-0.8Mn-0.5Ca legure nakon akumulativnog spajanja ekstruzijom kao nove metode intezivne plastične deformacije. Simulacija ovog postupka je pokazala da je prosečna efektivna deformacija po prolazu za kanale sa unutrašnjim uglom od 120 ᵒ iznosila oko 1,93. Prosečna veličina zrna je značajno smanjena sa 448,4 μm na 1,55 μm nakon tri prolaza. Posmatranje mikrostrukture ukazalo je da kombinacija kontinualne, diskontinualne i dvojnikovanjem izazvane dinamičke rekristalizacije predstavlja glavni mehanizam usitnjavanja zrna. Zatezna i pritisna čvrstoća su povećane sa 150 i 205 MPa na 330 i 301 MPa nakon tri prolaza akumulativnog spajanja ekstruzijom, što je ukazalo na 2 i 1,5 puta veće poboljšanje. Zatezno izduženje je smanjeno sa 26% za homogenizovani uzorak na 7,5% na uzorak koji je obrađen u tri prolaza zbog primetnog očvršćavanja, neujednačenih deformacija i nehomogene mikrostrukture nastale zbog akumulativnog spajanja ekstruzijom. Otpornost na koroziju u rastvoru SBF je poboljšana sa 1,1 na 14,159 KΩ Cm² nakon tri prolaza ovog postupka zbog prisustva hidroksilapatita koji je nastao na površini uzorka.

Ključne reči: Mg-0.8Mn-0.5Ca legura; Akumulativno spajanje ekstruzijom; Mikrostruktura; Mehanička svojstva; Korozija